PROCEEDINGS OF SPIE

SPIEDigitalLibrary.org/conference-proceedings-of-spie

Three-dimensional X-ray microscopy of zebrafish larvae

Osterwalder, Melissa, Bolten, Jan Stephan, Rodgers, Griffin, Schulz, Georg, Tanner, Christine, et al.

Melissa Osterwalder, Jan Stephan Bolten, Griffin Rodgers, Georg Schulz, Christine Tanner, Emre Cörek, Jörg Huwyler, Bert Müller, "Three-dimensional X-ray microscopy of zebrafish larvae," Proc. SPIE 11586, Bioinspiration, Biomimetics, and Bioreplication XI, 115860J (29 March 2021); doi: 10.1117/12.2583639

SPIE.

Event: SPIE Smart Structures + Nondestructive Evaluation, 2021, Online Only

Downloaded From: https://www.spiedigitallibrary.org/conference-proceedings-of-spie on 31 Mar 2021 Terms of Use: https://www.spiedigitallibrary.org/terms-of-use

Three-dimensional X-ray microscopy of zebrafish larvae

Melissa Osterwalder*[a,b], Jan Stephan Bolten[c], Griffin Rodgers[a,b], Georg Schulz[a,b,d], Christine Tanner[a,b], Emre Cörek[c], Jörg Huwyler[c], and Bert Müller[a,b]

[a]Biomaterials Science Center, Department of Biomedical Engineering, University of Basel, Gewerbestrasse 14, 4123 Allschwil, Switzerland
[b]Biomaterials Science Center, Department Clinical Research, c/o University Hospital Basel, Schanzenstrasse 55, 4031 Basel, Switzerland
[c]Division of Pharmaceutical Technology, Department of Pharmaceutical Sciences, University of Basel, Klingelbergstrasse 50, 4056 Basel, Switzerland
[d]Core Facility Micro- and Nanotomography, Department of Biomedical Engineering, University of Basel, Gewerbestrasse 14, 4123 Allschwil, Switzerland

ABSTRACT

Successful tomographic imaging of soft tissues with micrometer resolution includes preparation, acquisition, reconstruction, and data evaluation. Tissue preparation is essential for hard X-ray microtomography, because staining- and embedding materials can substantially alter the biological tissue *post mortem*. We performed tomographic imaging of zebrafish embryos in alcohol and after paraffin embedding with a conventional X-ray source and at a synchrotron radiation facility. The resulting multi-modal, three-dimensional data were registered for direct comparison. Single-cell precision was reached for the synchrotron radiation-based approach, which allows for segmentation of full organs such as the embryonic kidneys. While this approach offers an order of magnitude higher spatial resolution, many of the anatomical features can be readily recognized with the more accessible laboratory system. Propagation-based data acquisition enabled us to demonstrate the complementary nature of the edge-enhanced absorption contrast- and the phase contrast-based modality for visualizing multiple microanatomical features. While ethanol and paraffin embeddings allowed for identification of the same anatomical structures, paraffin-embedding, however, led to more artefacts and shrinkage. The presented multi-modal imaging approaches can be further extended to visualize three to four orders of magnitude larger volumes such as adult zebrafish or complete organs of larger animals such as mouse brains. Going towards even larger volumes, such as the human brain, presents further challenges related to paraffin embedding, data acquisition and handling of the peta-byte scale data volumes. This study provided a multi-modal imaging strategy by the combination of X-ray sources and sample embeddings which can play a role in addressing these challenges.

Keywords: Zebrafish embryo, hard X-ray computed tomography, synchrotron radiation source, conventional X-ray source, ethanol and paraffin embedding

1. INTRODUCTION

1.1 X-ray mictrotomography with synchrotron- and laboratory-based X-ray sources

Since RÖNTGEN's remarkable discovery of X-rays in the second half of the 19$^{\text{th}}$ century, they have been widely used for medical imaging purposes. The application fields of X-rays have vastly extended over the past decades even beyond the biomedical domain e.g. towards the material characterization of solid states or the investigation cultural heritage objects. A powerful strength of X-ray-based microtomography lies in the fact that the technique is label-free and physical slicing can be avoided due to the high penetration depth of hard X-rays. It further allows for three-dimensional imaging with isotropic voxels down to spatial resolutions of 1 µm or even below.

A simplified scheme of an X-ray microtomography setup is shown in Figure 1. It comprises three main components: the X-ray source which generates the X-ray beam, mostly in parallel beam geometry for synchrotron-radiation sources, as shown in the figure, and in cone beam geometry for laboratory sources. Next comes the

*melissa.osterwalder@unibas.ch, phone: +41 61 207 54 38, www.bmc.unibas.ch

Bioinspiration, Biomimetics, and Bioreplication XI, edited by Akhlesh Lakhtakia, Mato Knez, Raúl J. Martín-Palma,
Proc. of SPIE Vol. 11586, 115860J · © 2021 SPIE · CCC code: 0277-786X/21/$21 · doi: 10.1117/12.2583639

Downloaded From: https://www.spiedigitallibrary.org/conference-proceedings-of-spie on 31 Mar 2021
Terms of Use: https://www.spiedigitallibrary.org/terms-of-use

sample which is positioned on a rotation stage and ideally has a cylindrical shape. The last element is a detector unit, which here comprises a scintillator screen that converts the X-ray image into visible light, optical elements which magnify the optical image and finally a highly sensitive optical camera which digitally records the magnified image. In laboratory setups the use of flat panel detectors is more common. They also comprise a scintillator but then directly convert the light signal into electronic data that a computer can display as digital image while skipping the magnification step in between.

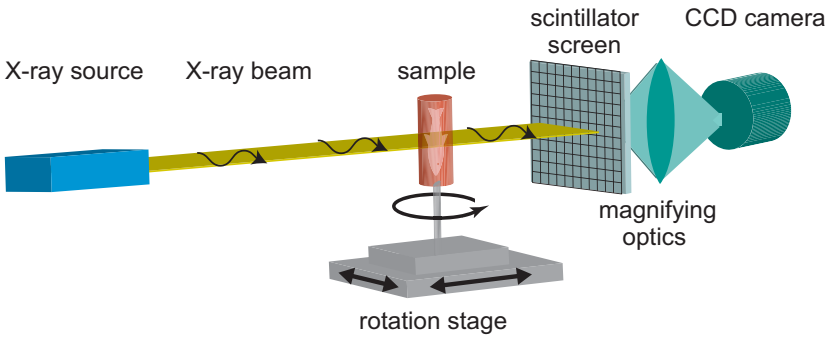

Figure 1. Scheme of the X-ray microtomography experiment. The X-ray source generates the X-ray beam in parallel- or cone beam geometry. The sample is integrated into a manipulator for sample positioning and movement. In this case the detection unit comprises a scintillator screen, magnifying optics and a CCD camera.

Here, only the first component, the X-ray source, shall be briefly discussed. In terms of beam properties, synchrotron radiation sources have some strong advantages over conventional systems. They offer highly brilliant radiation combined with a high flux that allows to select a photon energy by monochromatization, while maintaining a reasonably high intensity.[1,2] However, their accessibility for users is strongly restriced and usually requires successful beamtime proposals, which therefore impedes studies that rely on a high sample throughput or longitudinal studies. Conventional electron-impact X-ray sources, on the other hand, are limited in terms of brightness by the heat load that the target can tolerate and in terms of tunability. Their spectrum consists of a continuous spectrum of X-rays (bremsstrahlung) with some characteristic lines on top. However, conventional laboratory-based sources have the strong advantage that they can easily be integrated into cabinet-sized or even more compact desktop instruments, that can be operated at a local laboratory with high accessibility for the users.

In this study, we provide a direct comparison in performance for small soft tissue imaging between synchrotron- and laboratory-based X-ray microtomography. Three-day-old zebrafish embryos embedded in ethanol and paraffin were imaged with both a synchrotron radiation source and a conventional laboratory system. Precise alignment by three-dimensional image registration allows for a direct comparison of the datasets e.g. in terms of the identification of anatomical features, spatial resolution and image contrast.

1.2 The zebrafish embryo - a versatile vertebrate model organism

The zebrafish embryo is a well-established vertebrate model in various biomedical disciplines, including *in vivo* screenings for nanotoxicity or the analysis of the pharmacokinetics and targeting of nanocarriers.[3–5] It is a reliable alternative to human cell cultures or higher vertebrates as an *in vivo* model due to its high similarity in genetic profile, cell development and organ physiology with humans.[6] Further, as several genetic and environmental factors on social behaviour can be easily tuned, the organism has even emerged as valuable choice instead of rodents to study the determinants of social interactions.[7,8] Working with this organism is convenient because of its fast life cycle, easy husbandry, small size, optical transparency during early life stages and as no ethics approval is required for working with zebrafish embryos until five days post fertilization.

A preliminary synchrotron radiation-based micro computed tomography (SRμCT) study was performed to illustrate the feasibility to assess morphological changes of organs in zebrafish embryos throughout development or disease. As it has been previously shown that SRμCT is well suited to extract the cellular architecture of

Downloaded From: https://www.spiedigitallibrary.org/conference-proceedings-of-spie on 31 Mar 2021
Terms of Use: https://www.spiedigitallibrary.org/terms-of-use

zebrafish embryos throughout the entire organism,[9] we were confident towards the success of this approach. This study will be followed up by an ongoing research project, in which acute kidney injuries are induced in zebrafish embryos, causing acute cellular damage.[10,11] The anatomy of the pronephros of a two- to three-day-old zebrafish is shown in Figure 2 (*top left*). These simple kidneys consist of two bilaterally paired nephrons which are joined at their anterior ends by a central glomerulus, the blood filtering unit. The glomerulus is further connected to the pronephric ducts by the pronephric tubules.[12] The commonly used imaging technique to study the kidney's development is confocal laser scanning microscopy, which despite its strong advantage of being able to be performed *in vivo* it suffers from severe limitations such as a limited penetration depth, strong scattering and the need for transgenic organism. This technique can be complemented by SRμCT, providing the full three-dimensional anatomical context with isotropic micrometer resolution. On the bottom of Figure 2, we show a virtual slice through the dataset of an ethanol-embedded three-day-old zebrafish, where the features associated with the embryonic pronephros, namely the glomerulus (GL) and the proximal convoluted tubule (PCT) could be identified. Further, by a simple manual segmentation, a three-dimensional view of these structures is provided (*cf.* Fig. 2 *top right*). We are confident, that within this study it will be feasible to quantify the disease progress with e.g. degree of tubular and glomerular shrinkage, which are difficult to visualize by optical techniques. This will further validate and promote zebrafish embryos as a valid screening tool to assess nephrotoxicity as an alternative to vertebrates.

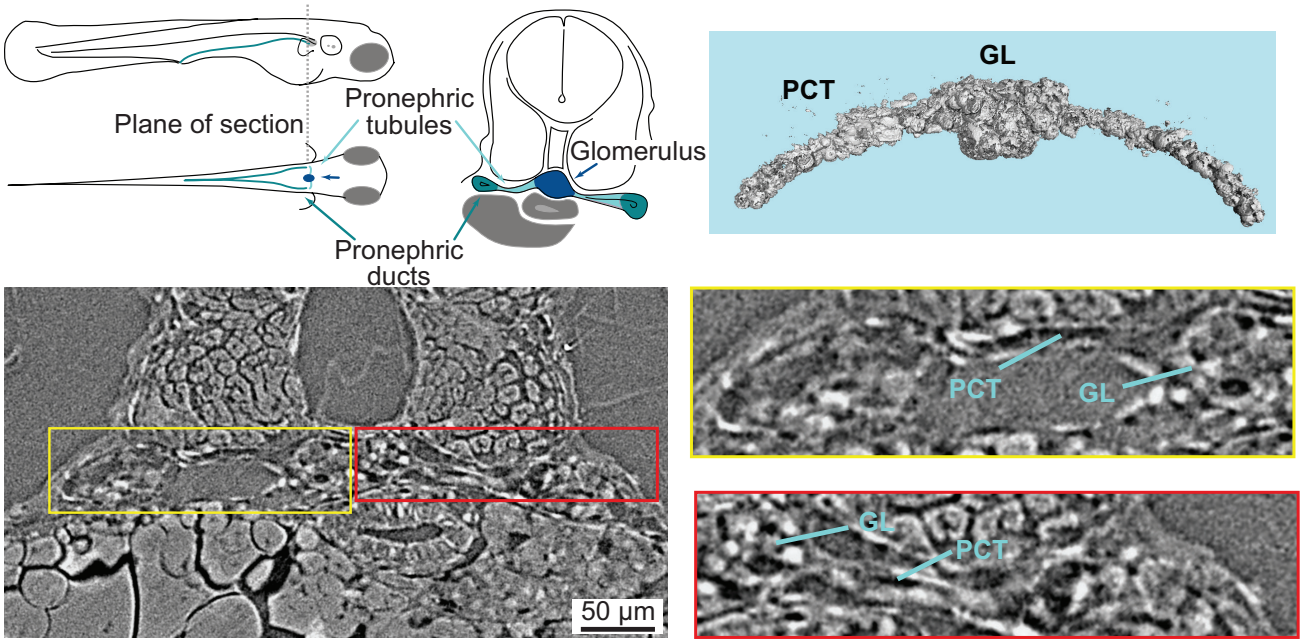

Figure 2. Visualization of zebrafish embryo kidneys in a preliminary SRμCT experiment. The pronephros of a two- to three-day-old zebrafish consists of a pair of nephrons connected at their anterior end by a central glomerulus (*top left*). Axial slice of a 72 hours post fertilization (hpf) larval zebrafish embedded in ethanol, taken at the plane of section indicated on top with 325 nm-wide isotropic voxels (*bottom left*). In a zoom-in view indicated by the yellow and red boxes, the glomerulus (GL) and the proximal convoluted tubule (PCT) can be identified (*bottom right*). By manual segmentation, a three-dimensional view on the glomerulus and the proximal convoluted tubule was extracted (*top left*).

Downloaded From: https://www.spiedigitallibrary.org/conference-proceedings-of-spie on 31 Mar 2021
Terms of Use: https://www.spiedigitallibrary.org/terms-of-use

2. METHODOLOGY

2.1 Preparation of zebrafish larvae

Zebrafish embryo embedding: The zebrafish embryos were euthanized 72 hours post fertilization (hpf) with tricaine methanesulfonate containing 0.612 mM trisaminomethane. Subsequently, they were fixed at room temperature in 4 % paraformaldehyde and stored at a temperature of 4 °C. Fixed specimens were dehydrated using ethanol at increasing concentrations (25 %, 50 %, 70 %, >99.5 %, 15 min each). For the paraffin embedding, the embryos fixed in ethanol were washed twice in xylene (> 98 %, Carl Roth, Switzerland) and further transferred into standard histological paraffin blocks (Leica paraplast bulk, USA) liquefied at a temperature of 68 °C. After cooling, cylinders were extracted from the paraffin block using a metal punches with inner diameters of 2.8 or 3.6 mm.

Sample housing: For the laboratory-based experiments, the ethanol-embedded zebrafish larvae were transferred with a micro-pipette to sample holders consisting of polyimide tubes (Polyimide-Tube AWG 20.5 NATUR, medical grade, Rotima AG, Stäfa, Switzerland) with an inner diameter of 0.762 mm and a wall thickness of 76.2 µm. The tubes were further sealed at both ends with BRAND^{TM} haematocrit sealing compound (Sigma-Aldrich, Wertheim, Germany) and two layers of nail polish.

For the synchrotron radiation-based experiments, the zebrafish larvae were placed within sample holders consisting of plastic pipettes filled with ethanol. For paraffin embedding, the paraffin blocks were manually trimmed in order to remove excess embedding material.

2.2 Micro computed tomography

Laboratory μCT: The samples were imaged by means of the commercially available dektop µCT scanner SkyScan 1275 (Bruker, Kontich, Belgium), equipped with a 3 Mp (1,944×1,536 pixels) CMOS flat panel detector. An effective pixel size of 4.2 µm, a tube voltage of 15 kVp, and a beam current of 156 µA were chosen for the tomography experiments. A total of 720 projections were acquired around 360°, with an exposure time of 2.2 s and 8 frames averaged, leading to total scan times of 3.5 h. Data processing and reconstruction was performed in an automated fashion using the dedicated `NRecon` Software (version 1.7.4). The datasets were cropped to remove background, resulting in final datasets with sizes ranging from 150 to 800 MB.

SRμCT: For the three-dimensional visualization of the zebrafish embryo anatomy single-distance phase-contrast (SDPC) microtomography was used. The experiments were performed at the TOMCAT X02DA beamline of the Swiss Light Source (Paul Scherrer Institut, Villigen, Switzerland).[13] A monochromatic beam with a photon energy of 12 keV was produced by a superbending magnet source combined with a Si(111) double crystal monochromator. For the detection of the projections, a LuAG:Ce scintillator coupled to a pco.EDGE 5.5 camera (2,560 × 2,160 pixel array, 16 bit depth) with the ULAPO20x objective were used to generate an effective pixel size of 325 nm. The propagation distance was set to 12 mm. Three height steps were acquired for visualization of the ethanol-embedded specimen and two height steps for the paraffin-embedded specimen. The exposure time was set to 200 ms for 2,000 projections recorded around 180°, resulting in scan times of approximately 8.5 minutes per height step.

Phase retrieval of the projections was performed based on the single-distance non-iterative method introduced by Paganin *et al.*[14] and carried out in `ImageJ` with the AnkaPhase plugin.[15] A δ/β-value of 50 was chosen to optimize contrast. Both absorption and phase contrast images were reconstructed with the Gridrec algorithm.[16]

2.3 Image registration

The reconstructed µCT-datasets of the (4 × 4 × 4)-binned synchrotron radiation-based measurements and the unbinned laboratory-based measurements were aligned using non-rigid registration based on B-spline transformations in `Elastix`[17,18] (version 5.0.0). The full-resolution SRµCT datasets were 62.4 GB for the ethanol-embedded sample and 34.8 GB for the paraffin-embedded sample and the laboratory µCT datasets were around 0.5 GB. For registration, the SRµCT datasets were (4 × 4 × 4)-binned and the data volume was further reduced by a factor of two by reducing the bit depth from 16 to 8 bit. Prior to the registration, an affine manual alignment was performed in `ITK-SNAP`[19] (version 3.8.0). The registration was divided in three steps, reducing the final grid spacing for the B-splines from 40 to 30 to 20 pixels (60 to 40 to 30 pixels for the registration shown in Figure 6).

Downloaded From: https://www.spiedigitallibrary.org/conference-proceedings-of-spie on 31 Mar 2021
Terms of Use: https://www.spiedigitallibrary.org/terms-of-use

Further, each step was subdivided into three resolutions, with a factor of two in between each step and the final resolution being given by the grid spacing. Masks were created *via* thresholding and morphological operations in `Matlab` (version R2020a). Optimization with respect to the mask regions used 1,000 iterations of adaptive stochastic gradient descent at each resolution. As similarity metric, the normalized correlation coefficient was chosen, which during initial tests based on visual inspection and tracking of image similarity provided a better alignment than mutual information or mean squared differences. The transformation was regularized by a bending energy penalty term with a weight of 10,000 (7,500 for Figure 6), which was determined by visual inspection of exploring a range of weights in initial tests.

3. RESULTS

Tomographic imaging with hard X-rays offers histology-like precision with a spatial resolution down to the micrometer scale or even below, while the necessary penetration depth is provided to overcome the limitation of sectioning. However, soft tissues mainly comprise low Z elements which generate hardly any contrast, as the X-ray attenuation coefficient follows a cubic law with atomic number. Therefore, it is often advantageous to make use of X-ray phase contrast modalities, especially for imaging unstained soft tissues, as the contrast advantage of phase, referring to the relation between the real and imaginary part of the refractive index, is around three orders of magnitude.[20] The most simple technique to assess the phase information of X-rays is by propagation-based imaging, where the sample is placed at a certain distance from the detector. It is based on the principle of Fresnel diffraction, where the interference between the deflected and the non-deflected wave leads to an edge enhancement.[21,22]

In Figure 3, the complementarity of the edge-enhanced absorption-information, shown on top, and the phase-information, shown at the bottom, are illustrated. To extract the phase information, single-distance phase retrieval with the method introduced by Paganin *et al.*[14] with a δ/β-ratio of 50 was employed. In a recent work, we have shown that a wealth of anatomical features can be identified by SRμCT of zebrafish larvae.[23] Here, we juxtapose two exemplary slices where both contrast modalities were extracted for an ethanol-embedded three-day-old zebrafish larva. Focusing on the zebrafish eye (*cf.* Fig. 3, *left*), we can identify the optic nerve (1) as well as several cell layers: the inner (2) and outer plexiform layer (4) and the ganglion cell layer (3). They can be distinguished much easier in the phase contrast image, however, we lose single-cell precision. In the edge-enhanced absorption image, even individual types of neurons such as the amacrine cells (5) and the bipolar cells (6) can be identified. Although some small features can be lost through blurring in single-distance phase retrieval, other features are only revealed by this increase in contrast. This is exemplified in Figure 3 on the right, showing a sagittal slice through the zebrafish embryo. While the embryonic heart (7) with the ventricle and the pericardial sac can be identified by both modalities e.g. the cerebellum (8) or the mandibular cartilage (9) remain hidden in the absorption modality due to insufficient contrast with respect to their surroundings.

Downloaded From: https://www.spiedigitallibrary.org/conference-proceedings-of-spie on 31 Mar 2021
Terms of Use: https://www.spiedigitallibrary.org/terms-of-use

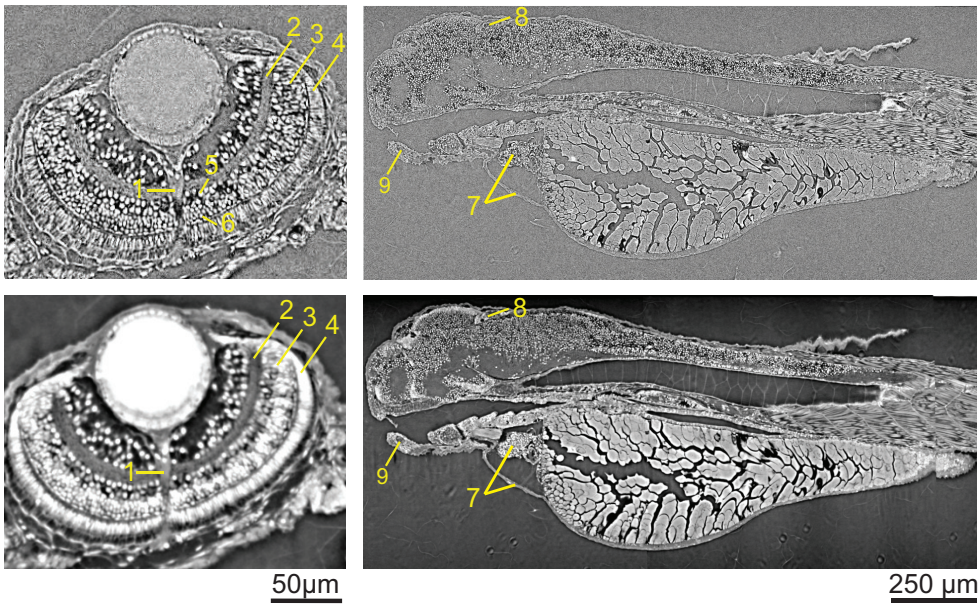

Figure 3. Complementarity of edge-enhanced absorption-based and phase-retrieved X-ray tomographic imaging. For two exemplary slices of a propagation-based imaging experiment, the extracted X-ray absorption- (*top*) and the phase-information (*bottom*) are shown. Labels for the highlighted anatomical features are provided in the legend and in the text.

Further, we directly compared the synchrotron- and laboratory-based approach for X-ray µCT of zebrafish larva. Therefore, the same specimen embedded in ethanol (*cf.* Fig. 4) and in paraffin (*cf.* Fig. 5) were first imaged with the rather simple conventional laboratory µCT system Skyscan 1275 with 4.2 µm-wide voxels and an estimated spatial resolution of 13 µm, determined by the method introduced by Mizutani *et al.*[24] Subsequently, they were imaged at the TOMCAT X02DA beamline of the Swiss Light Source in a propagation-based microtomography experiment with a monochromatized beam with an energy of 12 keV. The effective voxel size was 0.325 µm, corresponding to a spatial resolution of around 1.5 µm.

To achieve a good alignment between the two three-dimensional datasets, image registration was performed. After manual prealignment a multi-resolution registration with three grid spacings based on B-spline transformations was used as described in section 2.3. In Figures 4 - 6 three virtual slices in the axial (yellow-colored-frame), sagittal (red colored frame) and lateral (blue colored frame) plane of the $(4\times4\times4)$-binned synchrotron radiation-based dataset and their registered counterpart are shown at the locations indicated in the volume rendering. In Figure 4 the juxtaposed measurements are shown for ethanol embedding and in Figure 5 for paraffin embedding. Further, in Figure 6, the ethanol- and paraffin-embedded specimens, measured with the synchrotron radiation source were registered with respect to each other.

Downloaded From: https://www.spiedigitallibrary.org/conference-proceedings-of-spie on 31 Mar 2021
Terms of Use: https://www.spiedigitallibrary.org/terms-of-use

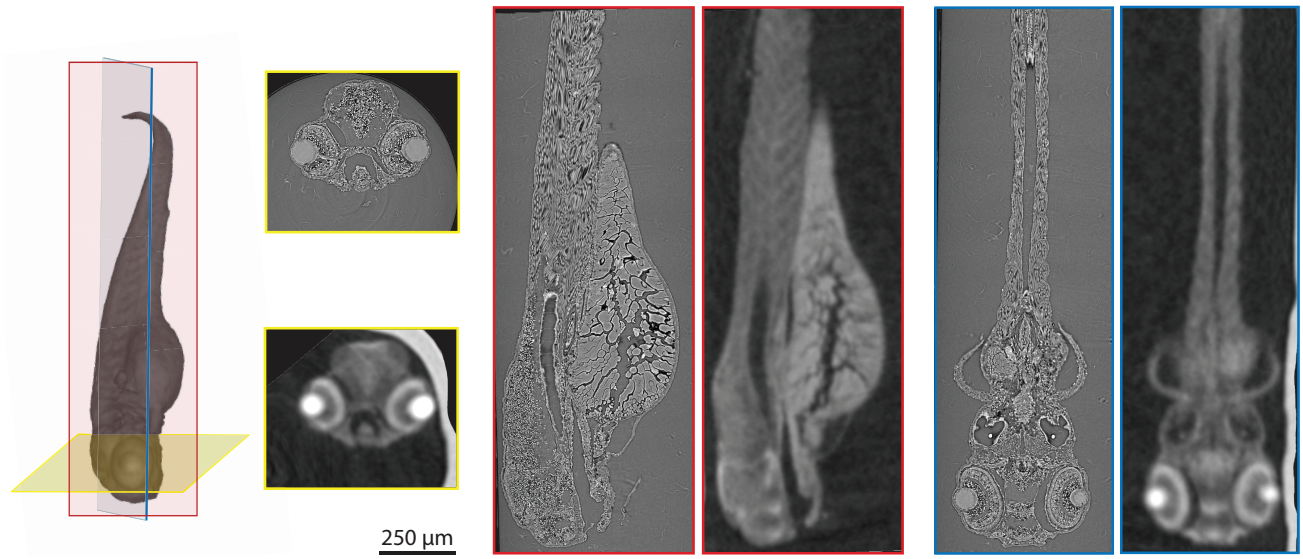

Figure 4. Direct comparison of synchrotron radiation-based X-ray µCT taken at the Swiss Light Source with a laboratory-based source. A three-day-old zebrafish larva embedded in ethanol was imaged at both the TOMCAT beamline of the Swiss Light Source and with the Skyscan 1275 system. The Skyscan dataset with 4.2 µm-wide isotropic voxels was registered to the TOMCAT dataset with 1.3 µm-wide voxels for better alignment. The section planes of the exemplary axial (yellow colored frame), sagittal (red colored frame) and lateral (blue colored frame) slices are indicated in the volume rendering.

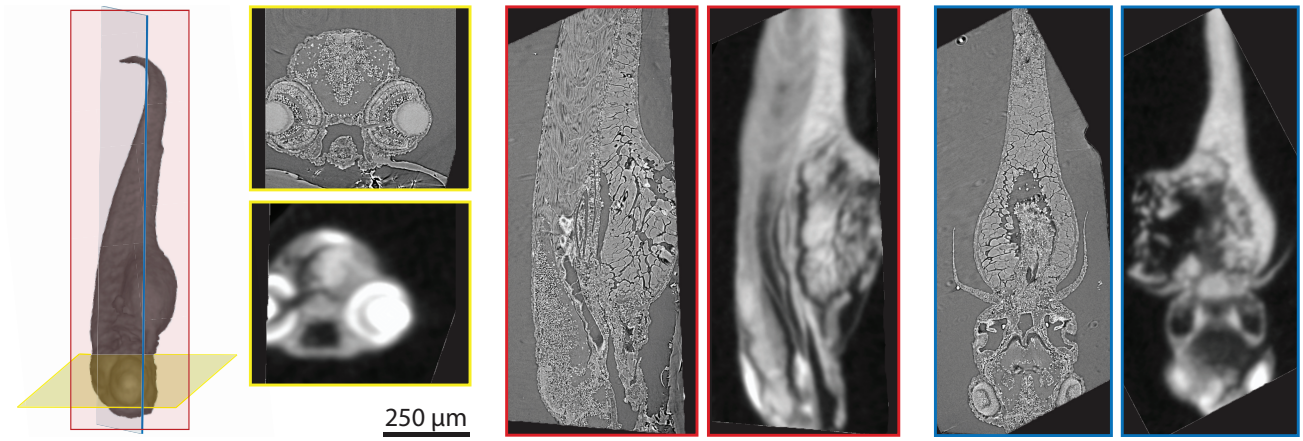

Figure 5. Direct comparison of SRµCT and laboratory-based µCT. A three-day-old zebrafish larva embedded in paraffin was imaged at both the TOMCAT beamline of the Swiss Light Source and with the Skyscan 1275 system. The Skyscan dataset with 4.2 µm-wide isotropic voxels was further registered to the TOMCAT dataset with 1.3 µm-wide voxels for better alignment. The section planes of the exemplary axial (yellow colored frame), sagittal (red colored frame) and lateral (blue colored frame) slices are indicated in the volume rendering.

Downloaded From: https://www.spiedigitallibrary.org/conference-proceedings-of-spie on 31 Mar 2021
Terms of Use: https://www.spiedigitallibrary.org/terms-of-use

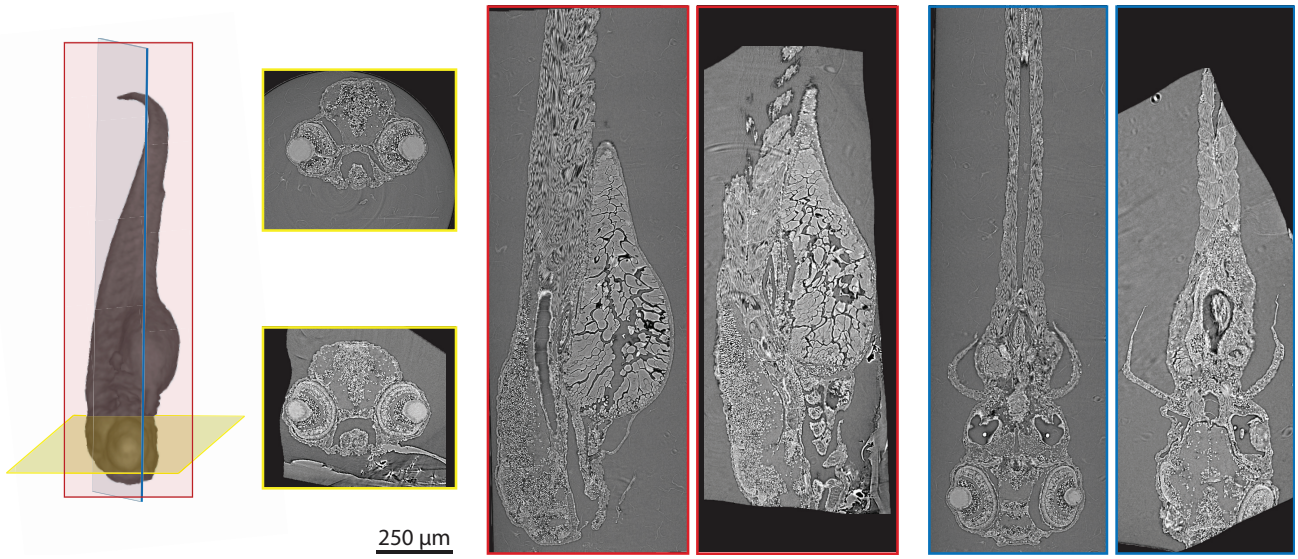

Figure 6. Direct comparison ethanol- and paraffin-embedding for SRµCT. Three-day-old zebrafish larva in ethanol and in paraffin were imaged at the TOMCAT beamline of the Swiss Light Source. The 4-fold binned synchrotron datasets in ethanol and paraffin were registered for better alignment. The section planes of the exemplary axial (yellow colored frame), sagittal (red colored frame) and lateral (blue colored frame) slices are indicated in the volume rendering.

Figure 7 allows to visually assess the alignment achieved by the registration process. In the middle row, a colorized overlay image of a lateral (*left*) and a sagittal slice (*right*) between the synchrotron radiation-based measurement (*top*) and the laboratory-based measurement (*bottom*) of a zebrafish larva in ethanol are shown. The SRµCT image is artificially colored in red and the laboratory-based image in green.

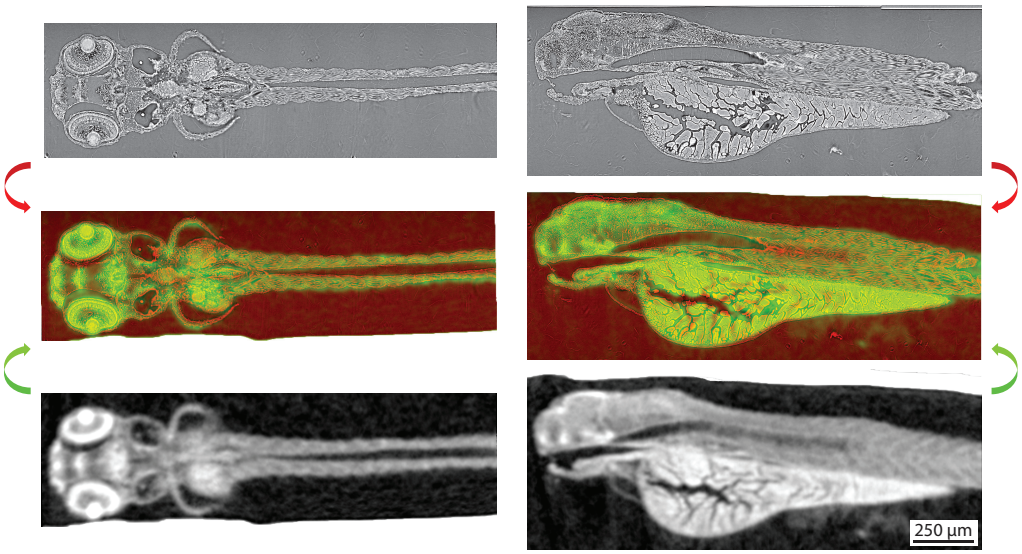

Figure 7. Visual assessment of three-dimensional image registration for a zebrafish larva in ethanol. The middle row shows an overlay of the synchrotron radiation-based measurement (*top*) and the laboratory-based measurement (*bottom*). The registration procedure included a manual prealignment, followed by a multi-grid and multi-resolution B-spline transformation. Details are provided in the text.

Downloaded From: https://www.spiedigitallibrary.org/conference-proceedings-of-spie on 31 Mar 2021
Terms of Use: https://www.spiedigitallibrary.org/terms-of-use

4. DISCUSSION

In this microtomography-based study, we have compared the performance of a rather simple conventional μCT system to a synchrotron radiation-based setup using zebrafish larvae in ethanol and paraffin. Despite the advantages of phase imaging, the interpretation of the gray values should be taken with care, because some assumptions for the phase retrieval are violated and the correct δ/β-ratio was not known *a priori*.[15,25]

SRμCT is an established technique for tomographic imaging of small soft tissues. However, numerous current research efforts are directed towards extending the technique for imaging of larger tissue samples or even entire organs. Thereby, a dominant research field is brain imaging in order to create human brain atlases. The best currently available atlas was created by the BigBrain project in 2013, which is based on over 7,000 full histological sections with 20 μm-wide voxels, resulting in a data size above 1 TB.[26] Creating a brain atlas based on SRμCT with micrometer resolution imposes many challenges to the researchers. An insight into some of the pillars and difficulties for realizing such a project shall be discussed with the help of Figure 8. For the zebrafish embryo, we have seen that SRμCT is clearly superior for identifying anatomical features compared to laboratory-based approaches. The strength of SRμCT for zebrafish embryo visualization has been demonstrated in a recent study, where the biodistribution of nanoparticles was assessed while providing the full anatomical context with isotropic resolution around 2 μm.[27] With a total volume of approximately 1 mm^3, even with sub-micron voxels, the raw datasets only occupy a few tens of GB. The multi-modal imaging approaches can be further extended to visualize hundreds of cubic millimeter volumes such as full organs of larger vertebrates. For the mouse brain, which has three orders of magnitude larger volume than the zebrafish embryo, the best currently available atlas is based on 450 μm-thick brain slices optically imaged with voxel sizes of 0.33 μm × 0.33 μm × 1.00 μm, which then already results in a roughly 8 TB raw volume.[28] Tomography data of the entire mouse brain with an isotropic pixel size of about 3 μm, see Fig. 8, exhibit also a few tens to hundreds of GB volumes. When going towards even larger volumes such as the human brain, which occupies a volume that is six to seven orders of magnitude larger than the zebrafish embryo, peta-byte scale data volumes of raw data are generated when maintaining true micrometer resolution. Another bottleneck is the limited field-of-view by the detector's dimensions. Currently available detectors consist of approximately 4000 × 4000 pixel arrays, limiting the field-of-view to only 4 mm when using 1 μm-wide effective pixels. There already exist various approaches for extending the field of view, e.g. by local tomography, where a tomogram is taken of only a small portion of the sample.[29] Other approaches are based on generating a mosaic projection (or sinogram) by stitching several limited field-of-view acquisitions prior to reconstruction,[30,31] which is referred to by some research teams by the term *tomosaic*.[32] However, all these approaches require significant computational resources for stitching and reconstruction of the big data and also precise translational stages. Recently, this approach has allowed for imaging a complete mouse brain with 0.8 μm-wide pixels, which was stitched on a mosaic grid of 12 × 11 images per projection.[32]

For the registration procedure, binning the SRμCT data was reasonable in order to reduce memory consumption and to better match the resolution of the laboratory μCT datasets. A non-rigid registration was necessary between the ethanol- and paraffin-embedded specimen to account for inter-sample variability and tissue shrinkage. Also for the comparison between the synchrotron radiation-based and the laboratory-based modalities it was a better choice than an affine registration, due to sample repositioning for the ethanol-embedded specimen and small morphological changes occurring with time. We observed that the registration performed best for the comparison of the specimen in ethanol, shown in Figure 4 & 7. The worse performance for paraffin embedding (*cf.* Fig. 5) may be attributed to the fact that the automatic method of mask generation was less reliable here and would have needed further manual adjustment. Further, the variety of gray values was much less for the Skyscan measurement in paraffin. For the registration between the ethanol- and paraffin embedded specimens which were imaged with the synchrotron-radiation source (*cf.* Fig. 6), achieving a good alignment was more difficult due to the large inter-individual variability and the morphology and contrast changes as well as damages from the preparation procedure.

Using laboratory X-ray sources for tomographic imaging of larger samples can be advantageous due to the cone-beam geometry. It allows for full-field illumination of objects with pixel sizes of up to 10^{-4} of the sample's diameter. In the right column of Figure 8, selected tomography slices of an entire human brain post mortem are presented. They have been acquired using the advanced μCT-system nanotom®m (GE Sensing & Inspection Technologies GmbH, Wunstorf, Germany). For paraffin embedding, serious challenges have to be mastered.

Downloaded From: https://www.spiedigitallibrary.org/conference-proceedings-of-spie on 31 Mar 2021
Terms of Use: https://www.spiedigitallibrary.org/terms-of-use

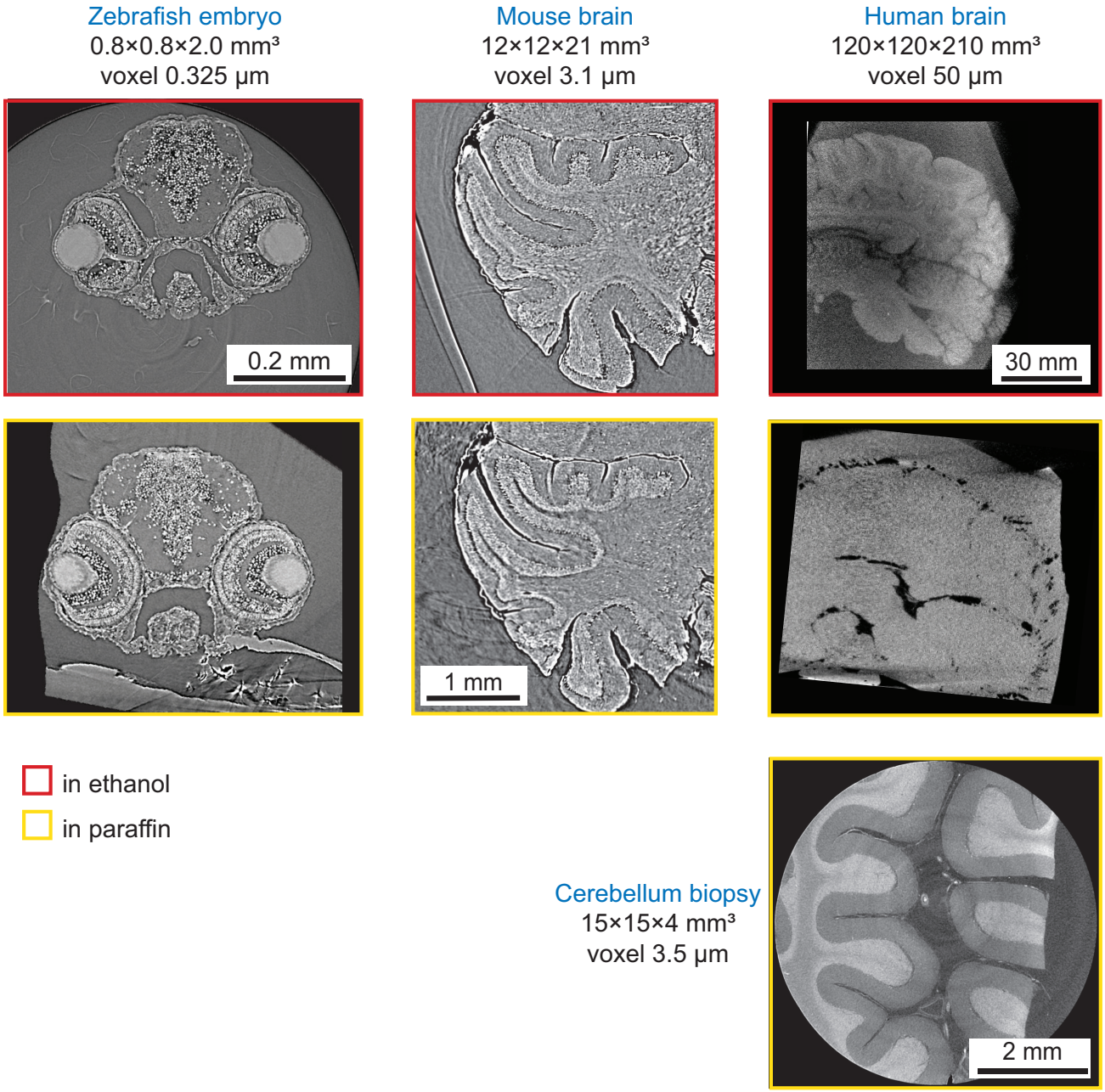

Figure 8. Embedding soft tissue samples over a range of length scales. Ethanol (red-colored frame) and paraffin embedding (yellow colored frame) are compared for a zebrafish embryo, measured at the TOMCAT beamline of the Swiss Light Source (*left*), a mouse brain measured at the ANATOMIX beamline of Synchrotron SOLEIL (*middle*) and an entire human brain measured with the laboratory system nanotom®m (GE Sensing & Inspection Technologies GmbH) (*right*). On the bottom a slice of a cerebellum biopsy measured with the same laboratory system is shown, illustrating that paraffin embedding of human brain tissues of millimeter or centimeter size could be performed successfully.

Downloaded From: https://www.spiedigitallibrary.org/conference-proceedings-of-spie on 31 Mar 2021
Terms of Use: https://www.spiedigitallibrary.org/terms-of-use

First, the contrast is surprisingly low. Second, air bubbles, originating from the embedding procedure, are causing prominent artefacts in phase-retrieved tomography. Achieving suitable paraffin embedding of an entire human brain is much more challenging than the embedding of smaller samples such as the human cerebellum. Substantial shrinkage during the solidification of paraffin requires the application of dedicated embedding protocols. Nevertheless, advanced μCT-systems such as the nanotom®m enabled us to identify non-stained cells in paraffin-embedded human cerebellum even in absorption-contrast mode. A representative slice of the paraffin-embedded human cerebellum displayed at the bottom of Figure 8 illustrates impressive contrast between the anatomical features. The substantially lower contrast in the images above is, therefore, attributed to the suboptimal preparation of the human brain for tomographic imaging.

5. CONCLUSION

So far, zebrafish embryos have been three-dimensionally visualized most commonly by means of optical methods. The optical methods are well suited, but also have limitations imposed by the penetration depth of the employed wavelength and by scattering at internal interfaces. Hard X-rays exhibit less interactions with matter and, selecting the suitable wavelength, even opaque tissues have been three-dimensionally visualized with isotropic resolution. Here, a spatial resolution below the optical limit was reached.[33] Therefore, it is meaningful to evaluate the performance of SRμCT for the microscopic imaging of zebrafish embryos in ethanol and paraffin. SRμCT allows for the identification of a wealth of anatomical features in zebrafish larvae down to the individual cells, but the access to synchrotron radiation facilities is limited. Hence, laboratory-based μCT measurements broaden the experimental basis, because many anatomical features can be readily made visible with an isotropic voxel size of a few microns. In order to allow for a direct comparison of the three-dimensional data from the selected modalities and samples after purposive preparation, non-rigid registration algorithms have to be implemented. Here, the zebrafish embryo data exemplifies the quality of registration pipelines. The results can only be partly extended to larger tissue samples such as entire murine and human brains. Whereas the size of the mouse brain still allows for suitable paraffin embedding and CT imaging with isotropic micron resolution, imaging the entire human brain requires dedicated developments for embedding and pipelines to treat data volumes in the petabyte range.

ACKNOWLEDGMENTS

The project was financially supported by the Swiss National Science Foundation (Project No. 185058). The authors acknowledge Dr. Christian Schlepütz for his active support during the beamtime No. 18949 at the TOMCAT X02DA beamline of the Swiss Light Source, PSI (Villigen, Switzerland). They further express their gratitude towards Dr. Anna Khimchenko for providing a tomography slice from the original dataset of the paraffin-embedded cerebellum imaged at the nanotom®m.

REFERENCES

[1] P. Willmott, "An Introduction to Synchrotron Radiation," *John Wiley & Sons Ltd.* , pp. 1–352, 2011.

[2] B. Hornberger, J. Kasahara, M. Gifford, R. Ruth, and R. Loewen, "A compact light source providing high-flux, quasi-monochromatic, tunable X-rays in the laboratory," *Proceedings of SPIE* **11110**(9), p. 2, 2019.

[3] F. Campbell, F. L. Bos, S. Sieber, G. Arias-Alpizar, B. E. Koch, J. Huwyler, A. Kros, and J. Bussmann, "Directing Nanoparticle Biodistribution through Evasion and Exploitation of Stab2-Dependent Nanoparticle Uptake," *ACS Nano* **12**(3), pp. 2138–2150, 2018.

[4] S. Sieber, P. Grossen, P. Detampel, S. Siegfried, D. Witzigmann, and J. Huwyler, "Zebrafish as an early stage screening tool to study the systemic circulation of nanoparticulate drug delivery systems in vivo," *Journal of Controlled Release* **264**, pp. 180–191, 2017.

[5] D. Witzigmann, P. Uhl, S. Sieber, C. Kaufman, T. Einfalt, K. Schöneweis, P. Grossen, J. Buck, Y. Ni, S. H. Schenk, J. Hussner, H. E. Meyer zu Schwabedissen, G. Québatte, W. Mier, S. Urban, and J. Huwyler, "Optimization-by-design of hepatotropic lipid nanoparticles targeting the sodium-taurocholate cotransporting polypeptide," *eLife* **8**, p. e42276, 2019.

Downloaded From: https://www.spiedigitallibrary.org/conference-proceedings-of-spie on 31 Mar 2021
Terms of Use: https://www.spiedigitallibrary.org/terms-of-use

[6] J. Jeevanandam, Y. S. Chan, and M. K. Danquah, "Zebrafish as a model organism to study nanomaterial toxicity," *Emerging Science Journal* **3**(3), pp. 195–208, 2019.
[7] S. Macrì and S. H. Richter, "The Snark was a Boojum - reloaded," *Frontiers in Zoology* **12**(1), p. S20, 2015.
[8] M. Karakaya, S. Macrì, and M. Porfiri, "Just like Star Trek, but a little less fancy: behavioral teleporting of live zebrafish," *Proceedings of SPIE* **11586**, p. 23, 2021.
[9] Y. Ding, D. J. Vanselow, M. A. Yakovlev, S. R. Katz, A. Y. Lin, D. P. Clark, P. Vargas, X. Xin, J. E. Copper, V. A. Canfield, K. C. Ang, Y. Wang, X. Xiao, F. D. Carlo, D. B. Rossum, P. L. Riviere, and K. C. Cheng, "Computational 3D histological phenotyping of whole zebrafish by x-ray histotomography," *eLife* **8**, pp. 1–28, 2019.
[10] K. K. McCampbell and R. A. Wingert, "New tides: Using zebrafish to study renal regeneration," *Translational Research* **163**(2), pp. 109–122, 2014.
[11] R. A. McKee and R. A. Wingert, "Zebrafish Renal Pathology: Emerging Models of Acute Kidney Injury," **3**(2), pp. 171–181, 2015.
[12] I. Drummond, "Making a zebrafish kidney: A tale of two tubes," *Trends in Cell Biology* **13**(7), pp. 357–365, 2003.
[13] M. Stampanoni, F. Marone, G. Mikuljan, K. Jefimovs, P. Trtik, J. Vila-Comamala, C. David, and R. Abela, "Broadband X-ray full field microscopy at a superbend," in *Journal of Physics: Conference Series*, **186**(1), p. 012018, 2009.
[14] D. Paganin, S. C. Mayo, T. E. Gureyev, P. R. Miller, and S. W. Wilkins, "Simultaneous phase and amplitude extraction from a single defocused image of a homogeneous object," *Journal of Microscopy* **206**(1), pp. 33–40, 2002.
[15] T. Weitkamp, D. Haas, D. Wegrzynek, and A. Rack, "ANKAphase : software for single-distance phase retrieval from inline X-ray phase-contrast radiographs," *Journal of Synchrotron Radiation* **18**(4), pp. 617–629, 2011.
[16] F. Marone and M. Stampanoni, "Regridding reconstruction algorithm for real-time tomographic imaging," *Journal of Synchrotron Radiation* **19**(6), pp. 1029–1037, 2012.
[17] S. Klein, M. Staring, K. Murphy, M. A. Viergever, and J. P. W. Pluim, "elastix: A Toolbox for Intensity-Based Medical Image Registration," *IEEE Transactions On Medical Imaging* **29**(1), pp. 196–205, 2010.
[18] D. P. Shamonin, E. E. Bron, B. P. Lelieveldt, M. Smits, S. Klein, and M. Staring, "Fast parallel image registration on CPU and GPU for diagnostic classification of Alzheimer's disease," *Frontiers in Neuroinformatics* **7**, p. 50, 2013.
[19] P. A. Yushkevich, A. Pashchinskiy, I. Oguz, S. Mohan, J. E. Schmitt, J. M. Stein, D. Zukić, J. Vicory, M. McCormick, N. Yushkevich, N. Schwartz, Y. Gao, and G. Gerig, "User-Guided Segmentation of Multi-modality Medical Imaging Datasets with ITK-SNAP," *Neuroinformatics* **17**(1), pp. 83–102, 2019.
[20] U. Bonse, "Röntgen-Mikrotomographie," *Physik Journal* **53**(3), pp. 211–214, 1997.
[21] P. Cloetens, M. Pateyron-Salomé, J. Y. Buffière, G. Peix, J. Baruchel, F. Peyrin, and M. Schlenker, "Observation of microstructure and damage in materials by phase sensitive radiography and tomography," *Journal of Applied Physics* **81**(9), pp. 5878–5886, 1997.
[22] A. Snigirev, I. Snigireva, V. Kohn, S. Kuznetsov, and I. Schelokov, "On the possibilities of x-ray phase contrast microimaging by coherent high-energy synchrotron radiation," *Review of Scientific Instruments* **66**(12), pp. 5486–5492, 1995.
[23] M. Osterwalder, J. S. Bolten, G. Rodgers, M. Humbel, G. Schulz, C. Tanner, J. Huwyler, and B. Müller, "Three-dimensional Hard X-ray microtomography of Zebrafish Larvae," *Proceedings of SPIE, Manuscript submitted for publication. doi:10.1117/12.2593119* , 2021.
[24] R. Mizutani, R. Saiga, S. Takekoshi, C. Inomoto, N. Naoyo, M. Itokawa, M. Arai, K. Oshima, A. Takeuchi, K. Uesugi, Y. Terada, and Y. Suzuki, "A method for estimating spatial resolution of real image in the Fourier domain," *Journal of Microscopy* **261**(1), pp. 57–66, 2016.
[25] T. Gureyev, S. Mohammadi, Y. Nesterets, C. Dullin, and G. Tromba, "Accuracy and precision of reconstruction of complex refractive index in near-field single-distance propagation-based phase-contrast tomography," *Journal of Applied Physics* **114**(14), p. 144906, 2013.

Downloaded From: https://www.spiedigitallibrary.org/conference-proceedings-of-spie on 31 Mar 2021
Terms of Use: https://www.spiedigitallibrary.org/terms-of-use

[26] K. Amunts, C. Lepage, L. Borgeat, H. Mohlberg, T. Dickscheid, M. É. Rousseau, S. Bludau, P. L. Bazin, L. B. Lewis, A. M. Oros-Peusquens, N. J. Shah, T. Lippert, K. Zilles, and A. C. Evans, "BigBrain: An ultrahigh-resolution 3D human brain model," *Science* **340**(6139), pp. 1472–1475, 2013.

[27] E. Cörek, G. Rodgers, S. Siegrist, T. Einfalt, P. Detampel, C. M. Schlepütz, S. Sieber, P. Fluder, G. Schulz, H. Unterweger, C. Alexiou, B. Müller, M. Puchkov, and J. Huwyler, "Shedding Light on Metal-Based Nanoparticles in Zebrafish by Computed Tomography with Micrometer Resolution," *Small* **16**(31), p. 2000746, 2020.

[28] A. Li, H. Gong, B. Zhang, Q. Wang, C. Yan, J. Wu, Q. Liu, S. Zeng, and Q. Luo, "Micro-optical sectioning tomography to obtain a high-resolution atlas of the mouse brain," *Science* **330**(6009), pp. 1404–1408, 2010.

[29] P. Kuchment, K. Lancaster, and L. Mogilevskaya, "On local tomography," *Inverse Problems* **11**(3), pp. 571–589, 1995.

[30] S. R. Stock, *Recent advances in X-ray microtomography applied to materials*, vol. 53, Taylor & Francis, 2008.

[31] A. Kyrieleis, V. Titarenko, M. Ibison, T. Connolley, and P. J. Withers, "Region-of-interest tomography using filtered backprojection: Assessing the practical limits," *Journal of Microscopy* **241**(1), pp. 69–82, 2011.

[32] R. Vescovi, M. Du, V. de Andrade, W. Scullin, D. Gürsoy, and C. Jacobsen, "Tomosaic: efficient acquisition and reconstruction of teravoxel tomography data using limited-size synchrotron X-ray beams," *Journal of Synchrotron Radiation* **25**(5), pp. 1478–1489, 2018.

[33] A. Khimchenko, C. Bikis, A. Pacureanu, S. E. Hieber, P. Thalmann, H. Deyhle, G. Schweighauser, J. Hench, S. Frank, M. Müller-Gerbl, G. Schulz, P. Cloetens, and B. Müller, "Hard X-Ray Nanoholotomography: Large-Scale, Label-Free, 3D Neuroimaging beyond Optical Limit," *Advanced Science* **5**(6), p. 1700694, 2018.

Downloaded From: https://www.spiedigitallibrary.org/conference-proceedings-of-spie on 31 Mar 2021
Terms of Use: https://www.spiedigitallibrary.org/terms-of-use